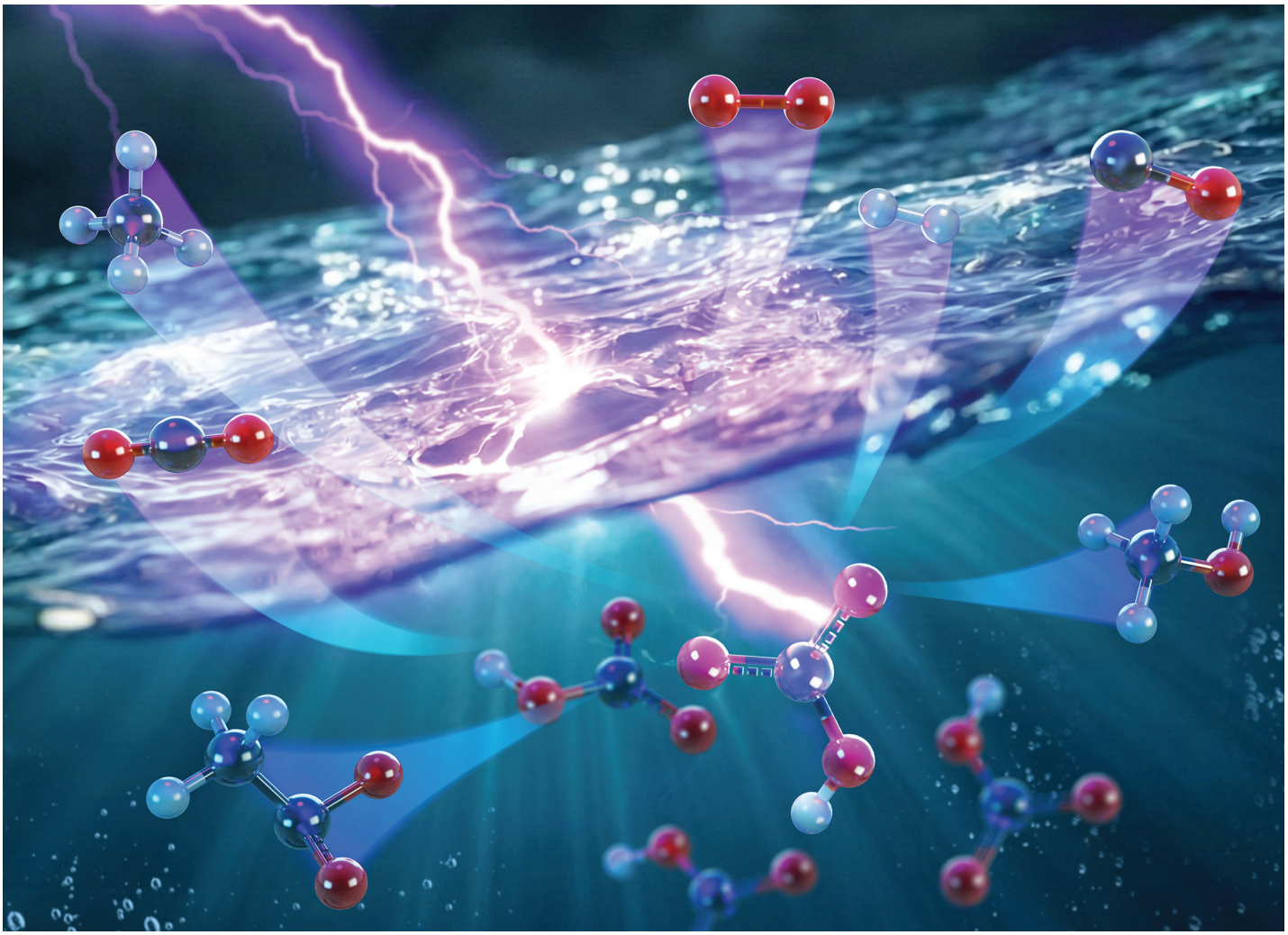

Showcasing research from Professor Y. Chris Li's laboratory, Department of Chemistry, University at Buffalo, USA.

Direct conversion of bicarbonate capture solution into multi-carbon products in a plasma electrochemical system

A plasma-catalytic process is reported to convert bicarbonate molecules into carbon monoxide and carbon dioxide. When paired with a subsequent electrochemical process, this platform enables the conversion of bicarbonate to ethylene with high Faradaic efficiency. This integrated plasma-electrochemical approach simplifies separate carbon capture and conversion steps, offering a more environmentally friendly process.

Image reproduced by permission of Yuguang C. Li from *Green Chem.*, 2026, **28**, 4466.

As featured in:

See Yuguang C. Li *et al.*, *Green Chem.*, 2026, **28**, 4466.

ROYAL SOCIETY OF CHEMISTRY

rsc.li/greenchem

Registered charity number: 207890

Green Chemistry

PAPER

View Article Online
View Journal | View Issue

Cite this: *Green Chem.*, 2026, **28**, 4466

Direct conversion of bicarbonate capture solution into multi-carbon products in a plasma electrochemical system

Xiaoli Ge,[a] Gina DelMonache,[a] Shwetha Prakash,[a] Mayuresh Janpandit,[a] Pratahdeep Gogoi,[a] Zhaoqiang Li[b] and Yuguang C. Li *[a]

Atmospheric CO_2 capture has become an increasingly important industrial process in response to climate challenges. Conventional CO_2 capture processes often require an energy-intensive step to regenerate the capture solution, typically a (bi)carbonate solution. Developing new chemical processes that directly convert the capture solution can bypass this energy-demanding regeneration step and yield valuable multi-carbon products. This study introduces a hybrid nonthermal plasma–electrochemical system that enables the direct conversion of bicarbonate molecules into ethylene in high yield. The captured bicarbonate solution is activated directly by solvated electrons and radical species generated from the plasma. The effects of counter cations in the HCO_3^- solution and carrier gas in the plasma reactor on the composition of plasma-activated intermediates, including O_2, H_2, CO, CO_2, and CH_4, were examined using NMR and GC/MS analyses. These mixed plasma-activated gaseous products, containing up to 73.5 vol% CO and CO_2, were subsequently introduced into an electrolyzer, achieving a C_{2+} faradaic efficiency of 83.7% at 200 mA cm^{-2} with 59.5% ethylene selectivity. This approach demonstrates the direct transformation of carbon capture solutions into high-yield C_{2+} products and establishes a platform for the chemical activation of otherwise inert molecules.

Received 9th October 2025,
Accepted 16th December 2025

DOI: 10.1039/d5gc05361g

rsc.li/greenchem

Green foundation

1. This work illustrated a new approach for the direct valorization of bicarbonate capture solution into ethylene. This approach simplifies two separate carbon capture and conversion steps and operates under ambient conditions completely, thereby minimizing both environmental impacts and energy consumption.
2. A faradaic efficiency of 83.7% was achieved when converting to C_{2+} products at −200 mA cm^{-2} with 59.5% ethylene selectivity – one of the highest selectivity performances for the direct conversion of bicarbonate into ethylene.
3. Future work will explore further improving energy efficiency and production throughput of the system. Technoeconomic analysis can be conducted to identify the pinch point of the system.

1. Introduction

As the global CO_2 level continues to rise due to industrial and human activities, environmental problems and energy crises are an ever-pressing problem for our society.[1–3] Therefore, capturing and converting atmospheric CO_2 into high-value chemicals has become a critical research area.[4] The electrochemical reduction of carbon dioxide, powered by renewable electricity, provides a promising approach to realizing carbon neutrality while generating highly valuable products and fuels, such as ethylene and ethanol.[5] However, industrial-scale CO_2 electrolyzers, despite their efficiency, require a CO_2 stream of high purity, which typically comes from CO_2 capture from air or an industrial flue gas stream. These processes demand significant energy input, especially for CO_2 regeneration such as that in drying and calcination processes.[4,6]

Considering energy consumption, researchers are exploring strategies to directly couple upstream CO_2 capture with a CO_2 conversion device, realizing *in situ* CO_2 regeneration and conversion from CO_2 capture products, such as bicarbonate or carbonate solution.[7–9] Compared with a gas-fed CO_2 electrolyzer, a liquid-fed (bi)carbonate electrolyzer can significantly reduce system complexity and approach high levels of CO_2 utilization. Li *et al.* developed a membrane electrode assembly (MEA) system based on a bipolar membrane (BPM) that can convert

[a]*Department of Chemistry, University at Buffalo, State University of New York, Buffalo, New York, 14260, USA. E-mail: yuguangl@buffalo.edu*
[b]*Department of Physics, Faculty of Arts and Sciences, Beijing Normal University, Zhuhai, Guangdong, 519087, P.R. China*

carbonate solution directly to produce pure syngas with a H_2 : CO ratio of *ca.* 3 : 1 and achieved 100% carbon utilization from the carbonate solution.[10] The operation of this device is based on the reaction between the proton generated from the BPM and the carbonate solution to produce CO_2 *in situ* locally on the catalyst's surface. Several follow-up studies have since investigated the influence of BPM, interlayer, or catalyst designs on the local pH with the goal of increasing the amount of *in situ* generated CO_2.[11–13] The Hatzell group demonstrated a Ni-based single-atom electrocatalyst integrated with a BPM-based MEA to directly convert bicarbonate into CO, achieving a 93% CO FE.[12] However, these (bi)carbonate electrolyzers still face some limitations. First, their selectivity for C_{2+} products is typically lower compared to conventional CO_2RR electrolyzers due to the low CO_2 concentration at the catalyst surface. Second, (bi)carbonate electrolyzers require a BPM or a cation exchange membrane (CEM) to generate or transport H^+ for CO_2 generation, which can increase the rate of the competing hydrogen evolution reaction. From a practical perspective, the dissociation of water within the BPM and the thickness of the BPM may lead to high overall cell voltages, which could pose challenges for scaling up. To continue advancing the field of direct bicarbonate conversion into value-added chemicals, new methods of activating bicarbonate solutions are needed.

In recent years, researchers have demonstrated the applications of non-thermal plasma technology in a number of different catalysis reactions under ambient conditions.[14–16] Non-thermal plasma or room-temperature plasma is typically generated *via* a dielectric barrier discharge mechanism, and it can activate thermodynamically stable molecules like CO_2 or N_2 into reactive species, allowing subsequent conversion into value-added compounds. For example, plasma conversion has been demonstrated by activating CH_4 or H_2 alongside CO_2 to generate hydrocarbons.[17–20] While plasma chemistry provides sufficient energy to break up any chemical bonds, reaction selectivity control is often very difficult. Therefore, incorporating catalysts into plasma reactors has been an ongoing research area to stabilize and facilitate the binding of reactants to steer the reaction outcome.[17,18,20] The continued development of plasma catalysis, especially in the direction of controlling reaction selectivity, could bring significant breakthroughs for catalysis science. Given the success of plasma CO_2 catalytic conversion, we posit that bicarbonate molecules, which are similar to CO_2 molecules, could also be activated *via* plasma and enable a new approach for direct bicarbonate solution conversion into value-added chemicals.

This work presents, for the first time, a new approach for coupling the plasma reactor with an electrolyzer to realize the reduction of plasma-activated bicarbonate, overcoming the limitations of *in situ* generated CO_2 concentration in the BPM-based bicarbonate electrolyzer. We employ a cascading plasma–electrochemical approach where the plasma reactor activates the bicarbonate solution, and the electrochemical reactor steers the reaction outcome with an optimally designed catalyst. This approach allows us to separately control the activation of bicarbonate and its reaction selectivity. In the plasma reactor, the bicarbonate solution was activated into H_2, O_2, CH_4, and CO_2, which were then used in the CO_2RR. The mechanism of HCO_3^- activation in the solution phase *vs.* gas phase concentration was investigated by studying the effects of concentration, cations paired with HCO_3^-, and the carrier gas in the plasma reactor on the composition of plasma-activated products. Under optimized plasma conditions, our continuous plasma–electrochemical system with a tandem CuAg electrocatalyst achieved a total C_{2+} FE of 83.7% at 200 mA cm^{-2}. To the best of our knowledge, this is one of the highest FE values for the direct conversion of bicarbonate solutions into C_{2+} products. These results highlight the potential of our plasma–electrochemical approach to separately control the reaction activation and selectivity of thermodynamically stable chemicals, enabling new pathways for other chemical transformations, such as methane oxidation or plastic upcycling.

2. Experimental

All chemicals were directly used as received without further purification. The anion exchange membrane (AEM) was purchased from the Fuel Cell Store. Potassium hydroxide (KOH), potassium bicarbonate ($KHCO_3$), and silver nitrate ($AgNO_3$) were obtained from Thermo Scientific. Ni foam was purchased from MTI Corporation.

Catalyst preparation

The Cu catalyst was prepared by sputtering a ~250 nm Cu layer on a polytetrafluoroethylene (PTFE) membrane using the Kurt J. Lesker Company PRO Line PVD 75. The CuAg bimetallic catalyst was synthesized by a galvanic exchange method. A piece of Cu-PTFE was immersed in 5 mL of a 5 mM $AgNO_3$ solution for 5 minutes at room temperature and then rinsed with deionized (DI) water and air dried.

Material characterization

Scanning electron microscopy (SEM) and energy-dispersive X-ray spectroscopy (EDS) images were obtained using the Carl Zeiss AURIGA CrossBeam. The surface compositions were analyzed using X-ray photoelectron spectroscopy (XPS) with a PHI 5000 VersaProbe. Mass spectra were acquired using an Agilent 6890 series gas chromatography system coupled with a 5973 mass selective detector. ^{1}H-NMR spectra were recorded using a Bruker 500 MHz system. Gas products were analyzed using gas chromatography (PerkinElmer, Clarus 590 GC) equipped with Carboxen 1000 and Mol Sieve 5A columns.

To evaluate radical formation under different cation electrolytes, 10 mM 2,2,6,6-tetramethylpiperidine 1-oxyl (TEMPO) was added to the plasma reactor under typical operational conditions. The concentration of the radicals generated from the plasma was extracted from electron spin resonance spectroscopy data.

Plasma reactor design

Our custom-made plasma reactor consists of a glass bottle as the main container, a saturated $KHCO_3$ solution as the reactant, a copper rod as the high-voltage electrode, and nickel foam as the ground electrode. The voltage profile of the plasma was measured with an oscilloscope and a high-voltage probe.

Electrochemical experiments

1.0 M KOH was used as both catholyte and anolyte and circulated with a peristaltic pump. The prepared Cu/CuAg-PTFE catalysts were applied as the cathode, Ni foam as the anode, and Ag/AgCl as the reference electrode. An anion exchange membrane (AEM) was placed between the anode and cathode. Electrochemical measurements were conducted using a SquidstatPlus Potentiostat (Admiral Instruments) in a flow cell. The CO_2RR was performed at current densities of −100, −200, −300, and −400 mA cm^{-2}. Different carrier gases from the plasma reactor were used as the inlet.

For the plasma production rate calculation (Fig. 2c–f and S6, S7), the H_2 and O_2 from the carrier gas were first subtracted. The inlet CO_2RR stream (the outlet of the plasma reactor) consists of a mixture of CO_2, CO, O_2, CH_4, and H_2, some of which are also products of the CO_2RR. The FE values reported in Fig. 3, 4 and S12 are calculated by subtracting the contributions of CO, CH_4, and H_2 from the plasma reaction; more specifically, GC measurements were conducted before every electrochemical CO_2RR to determine the amount of CO, CH_4, and H_2 from the plasma reaction. The CO, CH_4, and H_2 contributions from plasma are subtracted from the CO_2RR results to calculate the FE. For the stability test, a constant current density of −200 mA cm^{-2} was applied. The *j–V* curves were obtained through chronoamperometry experiments at different voltages for 5 minutes. The current densities averaged stable values in the final minute. All experiments were conducted in triplicate.

3. Results and discussion

The plasma–electrochemical system setup is illustrated in Fig. 1. Our custom plasma reactor is based on a dielectric barrier discharge mechanism and it is modified from previous reports.[21–23] A copper nail is used as the high-voltage electrode, while nickel foam acts as the ground electrode, facilitating plasma discharge at the HCO_3^- solution interface. The plasma-activated gas products were then purged into the flow cell for the CO_2RR. To maintain a stable flow rate for the CO_2RR, a carrier gas at 5 sccm was used to purge the plasma reactor bottle into the electrochemical reactor. As illustrated in Fig. S1a–c, during a plasma strike, visible vapor is generated inside the bottle. These vapors lead to plasma discharge in random orientation due to the water droplet next to the copper electrode creating a path for discharge. To maintain a consistent plasma output, we added a glass tube container around the copper electrode to constrain the plasma strikes, making them more concentrated towards the solution surface (Fig. S1d–f). Gas chromatography-mass spectrometry (GC-MS) and ^1H nuclear magnetic resonance (NMR) spectroscopy were applied to qualitatively identify the plasma-activated carbonaceous reactants in the gas and liquid phase, respectively. As shown in Fig. 2a and Fig. S2 and S3, O_2, CO, CO_2, and CH_4 were detected with GC-MS. H_2 was also detected with GC equipped with an FID detector (Fig. S2). These initial results confirm that plasma can efficiently activate the HCO_3^- molecule into smaller fragments. A plasma–electrochemical scheme will be a viable approach for the direct conversion of bicarbonate into value-added products. Given the plasma discharge at the HCO_3^- solution interface, the bicarbonate solution inside the plasma reactor was analyzed and methanol and acetate were identified (Fig. 2b). However, methanol and acetate remain in the bicarbonate solution bottle and do not participate in the subsequent electrochemical reaction.

Fig. S11 shows the time-dependent production rates of H_2, O_2, CH_4, and CO species, which exhibit excellent stability.

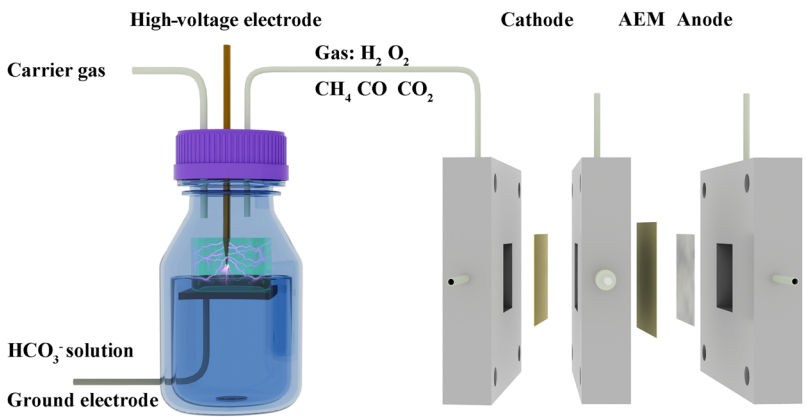

Fig. 1 Illustration of a continuous-flow plasma–electrochemical setup for bicarbonate activation. Bicarbonate ions are first activated in solution form; CO_2 is generated and then converted into ethylene in the subsequent electrochemical reactor.

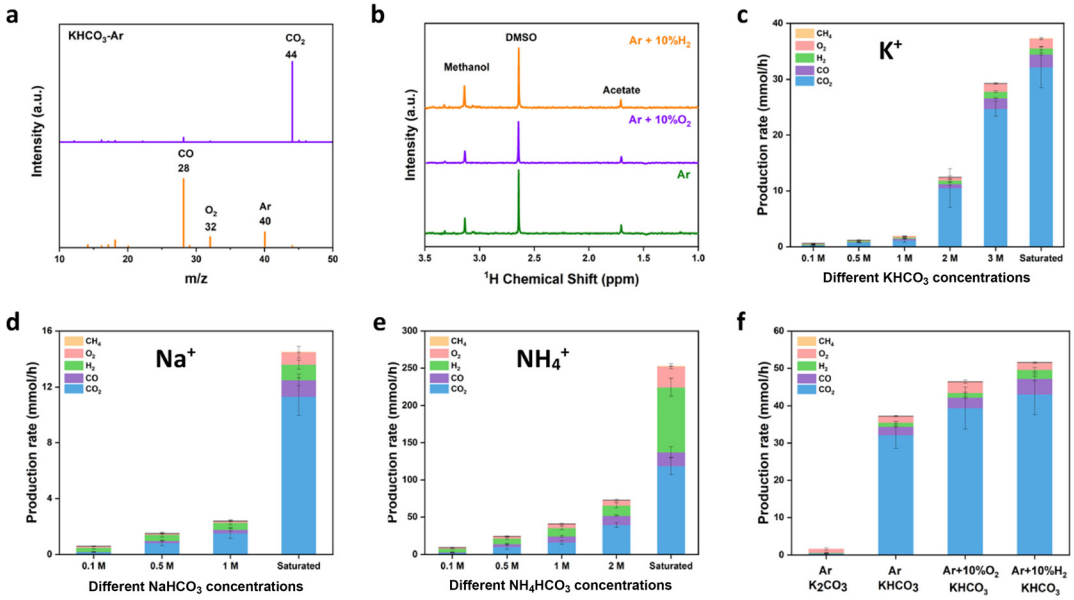

Fig. 2 (a) GC-MS spectra of plasma gas products under Ar with saturated $KHCO_3$ solutions. (b) ^{1}H-NMR of plasma gas products under different carrier gases with saturated $KHCO_3$ solutions. (c) Gas production rates under Ar with different $KHCO_3$ concentrations. (d) Gas production rates under Ar with different $NaHCO_3$ concentrations. (e) Gas production rates under Ar with different NH_4HCO_3 concentrations. (f) Gas production rates under different carrier gases with saturated $KHCO_3$ and K_2CO_3.

These results confirm that the plasma reactor is highly stable for continuous operation.

Isotopically labelled H, C and O experiments were conducted to identify the source of H, C and O. To identify the H source, for the electrochemically generated CH_4 and C_2H_4, we performed D_2O-labeling experiments by replacing the catholyte ($KOH + H_2O$) with $KOH + D_2O$ in the electrochemical reactor. As shown in Fig. S4, almost exclusive CD_4 (m/z = 20) and C_2D_4 (m/z = 32) are detected in GC/MS, suggesting that water is the hydrogen source in the electrolyte rather than the plasma-generated H_2. To determine the source of carbon in our products, we conducted ^{13}C-labeling experiments using $NaH^{13}CO_3$ as the electrolyte in the plasma reactor. As shown in Fig. S5a, only $^{13}CO_2$ (m/z = 45) is detected in the mass spectra, confirming that the C source is derived from HCO_3^- and ruling out any potential carbon contamination. To identify the O source in CO_2, we conducted ^{18}O-labeling experiments using $H_2{}^{18}O$ in the plasma reactor. As shown in Fig. S5b, the mass spectra reveal the presence of a mixture of $C^{16}O_2$ (m/z = 44), $C^{18}O^{16}O$ (m/z = 46), and $C^{18}O_2$ (m/z = 48), indicating that the O in CO_2 originates from both HCO_3^- and H_2O. This is consistent with the expectation that both bicarbonate and water molecules are broken up during plasma discharge.

Since the plasma discharge can interact with bicarbonate molecules either in solution or gas vapor phase, we first set out to investigate the impacts of different solutions and carrier gas conditions on the activation of bicarbonate under the plasma field. In the solution phase, we examine the HCO_3^- solution with different cations, K^+, Na^+, and NH_4^+, and quantify the respective plasma gas products. The yield of different species generated in the plasma reactor was quantified by GC at various concentrations of $KHCO_3$, $NaHCO_3$, and NH_4HCO_3, as shown in Fig. 2c–e. Under identical concentration conditions, the decomposition rate of HCO_3^- solution generally follows the trend of NH_4HCO_3 > $NaHCO_3$ > $KHCO_3$. If the salt concentrations are increased further, maximum production of CO_2 is reached in the saturated form of each solution. Of particular interest to note is that the decomposition rate of NH_4HCO_3 is orders of magnitude larger than that of $NaHCO_3$ and $KHCO_3$. The reported thermal decomposition temperatures of $KHCO_3$ and $NaHCO_3$ are well over 100 °C,[24,25] whereas the thermal decomposition temperature of NH_4HCO_3 is reported at *ca.* 30 °C.[26] Thus, the gas produced from plasma-activated NH_4HCO_3 has a large contribution from thermal decomposition. We conducted control experiments to determine the contribution of thermal decomposition in $KHCO_3$ and $NaHCO_3$. Fig. S9 reveals that only CO_2 was produced when heating a $NaHCO_3$ solution to 80 °C, with the production rate reaching less than 20% of that achieved *via* plasma activation. This suggests that CO_2 produced from $KHCO_3$ and $NaHCO_3$ are predominantly caused by plasma and to a small extent by thermal decomposition due to local temperature increases. The difference in the HCO_3^- solution decomposition rate when comparing Na^+ *vs.* K^+ may be attributed to the change in the solution dielectric constant due to cation disruption to the water network.[27]

To further evaluate the HCO_3^- activation mechanism, electron spin resonance (EPR) spectroscopy was conducted to probe the formation of plasma-generated radicals and to evaluate the relationship between different cations and radical generation. 2,2,6,6-Tetramethylpiperidine 1-oxyl (TEMPO) was used as a radical scavenger in the solution during the plasma reac-

tion; the amount of TEMPO consumed is a relative indicator of the radicals generated during the plasma reaction. As shown in Fig. S10, the TEMPO concentration in EPR follows a trend of $NH_4^+ < K^+ < Na^+$, indicating that the NH_4HCO_3 solution promotes the highest level of radical generation under plasma conditions, followed by K^+ and Na^+. This trend is consistent with the production rates of plasma-generated gaseous products, as shown in Fig. 2, and confirms the impact of cations in solution.

The solubilities of $KHCO_3$, $NaHCO_3$, and NH_4HCO_3 at room temperature are 3.3 M, 1.2 M, and 2.7 M, respectively. Thus, under saturated concentrations, the bicarbonate activation rate of $KHCO_3$ surpasses that of $NaHCO_3$. As shown in Tables S1 and S2, the saturated NH_4HCO_3 solution produced a higher amount of CO and CO_2 (137.38 mmol h^{-1}) compared to saturated $NaHCO_3$ and $KHCO_3$, but at the same time, it also produces a significant amount of hydrogen, reaching 33.1 vol% of the final gas outlet. The CO plus CO_2 concentration in the plasma reactor outlet was highest with saturated $KHCO_3$ at 92.4 vol% of the total gas produced without carrier gas, and 69.3 vol% with carrier gas. Details on the gas production rates are provided in Table S2. Consequently, a saturated $KHCO_3$ solution was selected as the carbon source for plasma activation in all subsequent experiments.

To investigate the gas-phase bicarbonate activation, we explored the effect of different carrier gases (Fig. 2f). Ar was originally chosen as a carrier gas due to its inertness. In this study, we introduced 10% H_2 and O_2 gases into the plasma reactor with Ar as two general reducing and oxidizing reactants to tune the outcome of the plasma products. The gaseous species observed under Ar with 10% O_2 and Ar with 10% H_2 were similar to those detected under pure Ar. However, the production rates varied significantly. In particular, the production rate of CO_2 (Table S3) under Ar with 10% H_2 approached 43.11 mmol h^{-1}, which is 34% higher than pure Ar. The amount of CO and H_2 was also higher than the Ar baseline. The CO plus CO_2 concentration in the outlet of the plasma reactor with saturated $KHCO_3$ under Ar with 10% H_2 (Table S4) reached a maximum of 73.5 vol% with carrier gas. The addition of H_2 in the plasma gas stream likely stabilizes the OH^- product from the dissociation of bicarbonate ($HCO_3^- \rightarrow CO_2 + OH^-$), thus promoting the overall bicarbonate activation and CO_2 production. The activation of carbonate solution under Ar was also tested under similar plasma conditions; however, the CO_2 production rate is much lower than that of saturated $KHCO_3$ solution, likely due to the higher stability of K_2CO_3.

As demonstrated by the results thus far, bicarbonate ions can be effectively activated into CO_2 by plasma activation. Given these findings, we conducted a CO_2RR experiment using a Cu-PTFE catalyst in a flow cell setting with 1 M KOH electrolyte. Cu was chosen as it is the only catalyst effective toward C_{2+} products.[28–31] A baseline CO_2RR was first established using pure CO_2 from a gas cylinder to confirm the Cu catalyst product distribution under control conditions. As illustrated in Fig. 3a, the Cu-PTFE catalyst exhibited high CO_2RR selectivity while suppressing the competitive HER. At current densities of −100, −200, −300, and −400 mA cm^{-2}, the FE values of the C_{2+} products were 73.5%, 79.5%, 73.6%, and 61.4%, respectively, consistent with prior reports.[32,33] Subsequently, the plasma-activated CO_2 was connected directly to the flow cell without any treatment and its performance is shown in Fig. S12. However, under this condition, CH_4 and H_2 were detected as major products. We posit that the water content in the plasma products participated in the reduction reaction directly leading to hydrogen evolution. Additionally, excess water content reduced the CO_2 concentration, leading to CH_4 production, as suggested by previous reports on CO_2 concentration effects.[34,35]

To mitigate the impacts of water, we reevaluated the CO_2RR using a Drierite drying column in the gas line between the plasma outlet and the electrochemical reaction cell, with the obtained results shown in Fig. 3b. A maximum FE towards C_{2+} of 72.6% was achieved at −200 mA cm^{-2}, which is within the standard deviation error of the control using pure CO_2 (Fig. 3a). The small difference in performance may be due to the trace amount of water left in the gas stream. With the 10% H_2 in the Ar carrier gas from the plasma reactor, the C_{2+} FE increased further to 82.6% at −200 mA cm^{-2} (Fig. 3d). The improvement is likely due to the presence of CO in the gas stream, which is a key intermediate during the CO_2RR towards C_{2+} products. The FE performance of our plasma–electrochemical system matched or exceeded that of the baseline CO_2RR FE obtained with pure CO_2. It is also one of the best performances for direct bicarbonate conversion into ethylene in a CO_2 electrolyzer.

To eliminate concerns that plasma-generated methanol and acetate may evaporate and dissolve into the catholyte to influence the accuracy of the CO_2RR FE, we conducted a controlled experiment by running our plasma–electrochemical system for 30 minutes without applying any current/voltage to the electrochemical cell. The catholyte was then collected and analyzed by ^{1}H-NMR spectroscopy. As shown in Fig. S13, when there is no electrochemical reaction, no detectable methanol or acetate signals were observed.

To probe the reaction kinetics, electrochemical impedance spectroscopy (EIS) was applied to investigate the kinetic differences between plasma-activated bicarbonate *vs.* pure CO_2 gas-fed electrolyzers. As demonstrated in Fig. 4a, the R_s values across all conditions were similar within experimental errors. However, all plasma-activated conditions exhibited significantly lower charge transfer resistance (R_{ct}) values compared to pure CO_2 gas-fed condition, indicating that the presence of mixed gases has enhanced the reaction kinetics. The fitted parameters and the equivalent circuit model for the EIS curves are provided in Table S6. The *j–V* curves for all conditions are shown in Fig. 4b. All voltages reported here are half-cell voltages *versus* the Ag/AgCl reference electrode without *iR* correction. Compared to the CO_2-fed conditions, plasma-activated systems exhibited a positive shift in onset potential from −1.1 V to −0.7 V (see inset in Fig. 4b), indicating favorable reaction kinetics similar to the EIS results. This has likely been contrib-

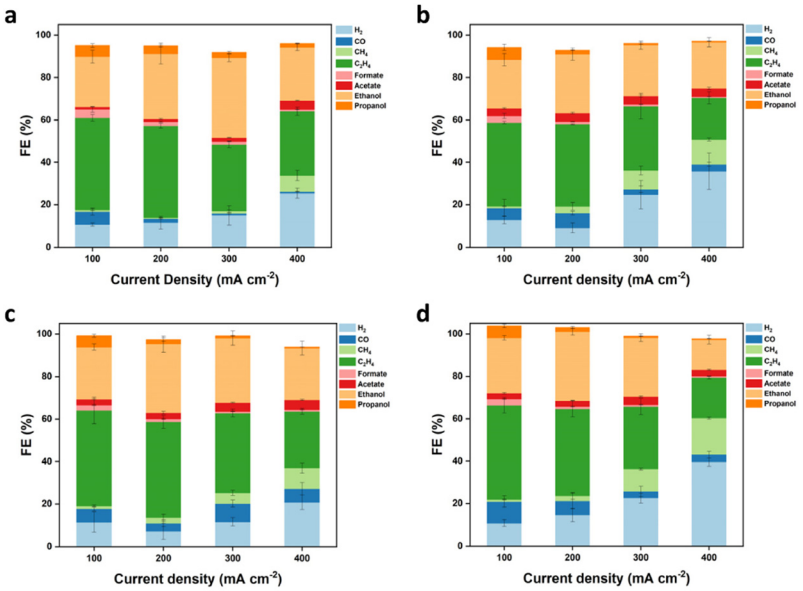

Fig. 3 The CO_2RR FE of a sputtered Cu catalyst under different conditions. (a) Pure CO_2. (b) Plasma-generated gases with Ar. (c) Plasma-generated gases with Ar + 10% H_2. (d) Plasma-generated gases with Ar + 10% O_2.

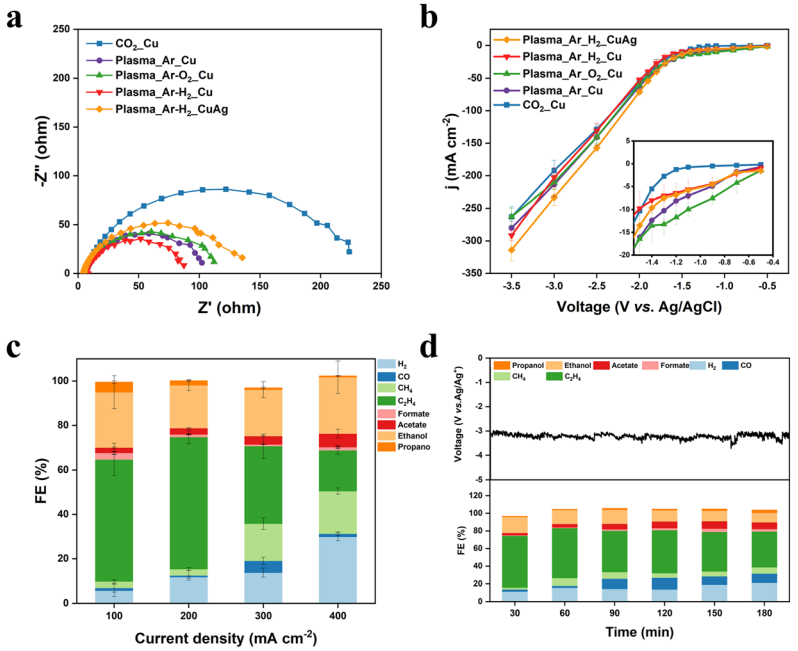

Fig. 4 (a) EIS spectra for the different CO_2RR conditions. (b) The *j*–*V* curves for different CO_2RR conditions in the voltage range of −0.5 to −3.5 V *vs.* Ag/AgCl, with the inset showing the enlarged *j*–*V* curves in the voltage range of −0.5 to −1.5 V *vs.* Ag/AgCl. (c) The FE for plasma-generated CO_2 with 90% Ar + 10% H_2 carrier gases and CuAg alloy prepared by the galvanic replacement reaction. (d) The stability test for the plasma–electrochemical configuration.

uted by the addition of CO in the gas stream, as CO_2 conversion into CO is often considered the rate-limiting step.[36]

As illustrated in the electrochemical results, the abundance of CO* and CO-related intermediates can effectively enhance the CO_2RR toward C_{2+} products. Alloying Cu with CO-selective metals (*e.g.*, Au, Ag, Zn) has been demonstrated to facilitate a sequential CO_2-to-CO conversion for more efficient C–C coupling.[37–40] To further enhance the FE for C_{2+} products, a CuAg bimetallic alloy was prepared *via* the galvanic substitution method. Representative scanning electron microscopy (SEM) and energy-dispersive X-ray spectroscopy (EDS) images (Fig. S14 and 15) confirmed the homogeneous distribution of Cu and Ag

in Cu-PTFE and CuAg-PTFE catalysts. X-ray photoelectron spectroscopy (XPS) provided further insight into the composition and electronic structure of synthesized Cu-PTFE and CuAg-PTFE. The Cu 2p spectra of Cu-PTFE (Fig. S16) exhibited two major peaks at 933.2 eV and 952.0 eV with a 2 : 1 area ratio, representing Cu $2p_{3/2}$ and Cu $2p_{1/2}$. The peaks at 934.4 eV and 955.2 eV were ascribed to Cu^{2+} species. These oxidized species were formed due to air exposure, which will be reduced to the metallic states under our electrochemical process. After alloying with Ag, the Cu 2p spectra (Fig. S17a) exhibited a positive shift, indicating altered surface electronic states. The Ag 3d XPS spectra (Fig. S17b) of CuAg-PTFE revealed peaks at 367.8 eV and 373.8 eV, corresponding to Ag $3d_{5/2}$ and Ag $3d_{3/2}$, respectively. Fig. 4c demonstrates the CO_2RR FE for the CuAg-PTFE, achieving a C_{2+} FE of 83.7% at a current density of −200 mA cm^{-2} with C_2H_4 as the dominant product, reaching a selectivity of 59.5%. To evaluate the overall plasma–electrochemical system stability, a constant current experiment at −200 mA cm^{-2} was conducted with gas products from the plasma reactor. Gas and liquid products from the CO_2RR were collected every 30 minutes for product analysis. As illustrated in Fig. 4d, the system maintained a C_{2+} FE of 62.3% after 180 minutes, demonstrating good operational stability. For comparison, we compiled recent reports on direct bicarbonate to C_{2+} conversion in Table S7. Notably, our plasma-activated bicarbonate method achieves the highest FE for C_{2+} products.[41–48] At the same time, we do acknowledge that our current energy efficiency is not sufficiently impactful and it is an area of improvement that we are actively working on.

4. Conclusions

The current work demonstrates a hybrid plasma–electrochemical system to enable the *ex situ* activation of bicarbonate solutions and optimization of the gas-phase composition for electrochemical CO_2 reduction. This approach provides an alternative route for direct bicarbonate conversion into value-added products compared to a BPM-based electrolyzer. The CO_2-to-C_{2+} selectivity is enhanced due to the addition of CO to the CO_2 stream, promoting C–C coupling. Under optimized plasma conditions with saturated $KHCO_3$ and Ar + 10% H_2, a maximum CO/CO_2 concentration of 73.5% was achieved in the plasma reactor output. When coupled with a CO-selective CuAg-PTFE catalyst, the continuous plasma–electrochemical system realized a record C_{2+} FE of 83.7% at −200 mA cm^{-2} with C_2H_4 selectivity reaching 59.5%. This plasma–electrochemical system can provide utilities beyond CO_2 reduction to facilitate the electrochemical synthesis of otherwise difficult-to-activate species, such as CH_4, N_2, or polymeric compounds, providing a new pathway to realize a carbon-neutral economy.

Author contributions

Y. C. L. and X. G. conceptualized the idea of this project. The manuscript was written through contributions of all authors. All authors have given approval to the final version of the manuscript.

Conflicts of interest

There are no conflicts to declare.

Data availability

The data that support this study are available within the article and its supplementary information (SI). Supplementary information: material synthesis and characterization studies, plasma reactor design, electrochemical experiments, Fig. S1–S17, and Tables S1–S7. See DOI: https://doi.org/10.1039/d5gc05361g.

Acknowledgements

Y. C. L. would like to thank the Research Corporation for Science Advancement for funding support through the Cottrell Scholar Award.

References

1 W. Lai, Z. Ma, J. Zhang, Y. Yuan, Y. Qiao and H. Huang, *Adv. Funct. Mater.*, 2022, **32**, 2111193.
2 W. Lai, Y. Qiao, J. Zhang, Z. Lin and H. Huang, *Energy Environ. Sci.*, 2022, **15**, 3603–3629.
3 S. Jin, Z. Hao, K. Zhang, Z. Yan and J. Chen, *Angew. Chem.*, 2021, **133**, 20795–20816.
4 D. W. Keith, G. Holmes, D. S. Angelo and K. Heidel, *Joule*, 2018, **2**, 1573–1594.
5 J. E. Huang, F. Li, A. Ozden, A. Sedighian Rasouli, F. P. García de Arquer, S. Liu, S. Zhang, M. Luo, X. Wang and Y. Lum, *Science*, 2021, **372**, 1074–1078.
6 S. Liu, J. Zhang, F. Li, J. P. Edwards, Y. C. Xiao, D. Kim, P. Papangelakis, J. Kim, D. Elder and P. De Luna, *Energy Environ. Sci.*, 2024, **17**, 1266–1278.
7 D. J. Pimlott, Y. Kim and C. P. Berlinguette, *Acc. Chem. Res.*, 2024, **57**, 1007–1018.
8 Q. Xia, K. Zhang, T. Zheng, L. An, C. Xia and X. Zhang, *ACS Energy Lett.*, 2023, **8**, 2840–2857.
9 A. Ozden, F. P. García de Arquer, J. E. Huang, J. Wicks, J. Sisler, R. K. Miao, C. P. O'Brien, G. Lee, X. Wang and A. H. Ip, *Nat. Sustainability*, 2022, **5**, 563–573.
10 Y. C. Li, G. Lee, T. Yuan, Y. Wang, D.-H. Nam, Z. Wang, F. P. García de Arquer, Y. Lum, C.-T. Dinh and O. Voznyy, *ACS Energy Lett.*, 2019, **4**, 1427–1431.
11 G. Lee, A. S. Rasouli, B.-H. Lee, J. Zhang, Y. C. Xiao, J. P. Edwards, M. G. Lee, E. D. Jung, F. Arabyarmohammadi and H. Liu, *Joule*, 2023, **7**, 1277–1288.
12 H. Song, C. A. Fernández, H. Choi, P.-W. Huang, J. Oh and M. C. Hatzell, *Energy Environ. Sci.*, 2024, **17**, 3570–3579.

13 Z. Zhang, D. Xi, Z. Ren and J. Li, *Cell Rep. Phys. Sci.*, 2023, **4**, 101662.
14 A. George, B. Shen, M. Craven, Y. Wang, D. Kang, C. Wu and X. Tu, *Renewable Sustainable Energy Rev.*, 2021, **135**, 109702.
15 J. Knezevic, T. Zhang, R. Zhou, J. Hong, R. Zhou, C. Barnett, Q. Song, Y. Gao, W. Xu and D. Liu, *J. Am. Chem. Soc.*, 2024, **146**, 12601–12608.
16 X. Ge, C. Zhang, M. Janpandit, S. Prakash, P. Gogoi, D. Zhang, T. R. Cook, G. I. Waterhouse, L. Yin and Z. Wang, *J. Am. Chem. Soc.*, 2024, **146**, 35305–35312.
17 L. Dou, Y. Liu, Y. Gao, J. Li, X. Hu, S. Zhang, K. K. Ostrikov and T. Shao, *Appl. Catal., B*, 2022, **318**, 121830.
18 N. Joshi and S. Loganathan, *ACS Omega*, 2023, **8**, 13410–13420.
19 C. De Bie, J. van Dijk and A. Bogaerts, *J. Phys. Chem. C*, 2016, **120**, 25210–25224.
20 S. Meng, L. Wu, M. Liu, Z. Cui, Q. Chen, S. Li, J. Yan, L. Wang, X. Wang and J. Qian, *AIChE J.*, 2023, **69**, e18154.
21 H. Zeghioud, P. Nguyen-Tri, L. Khezami, A. Amrane and A. A. Assadi, *J. Water Process Eng.*, 2020, **38**, 101664.
22 C. A. Aggelopoulos, *Chem. Eng. J.*, 2022, **428**, 131657.
23 G. T. Bae, J. Y. Kim, D. Y. Kim, E. Y. Jung, H. J. Jang, C.-S. Park, H. Jang, D. H. Lee, H.-K. Lee and H.-S. Tae, *Materials*, 2021, **14**, 7559.
24 M. Hartman, K. Svoboda, B. r. Čech, M. Pohořelý and M. Šyc, *Ind. Eng. Chem. Res.*, 2019, **58**, 2868–2881.
25 R. S. Gärtner, M. M. Seckler and G.-J. Witkamp, *Ind. Eng. Chem. Res.*, 2005, **44**, 4272–4283.
26 P. Nowak and J. Skrzypek, *Chem. Eng. Sci.*, 1989, **44**, 2375.
27 G. Das, S. Hlushak, M. C. Dos Ramos and C. McCabe, *AIChE J.*, 2015, **61**, 3053–3072.
28 D. Raciti and C. Wang, *ACS Energy Lett.*, 2018, **3**, 1545–1556.
29 G. L. De Gregorio, T. Burdyny, A. Loiudice, P. Iyengar, W. A. Smith and R. Buonsanti, *ACS Catal.*, 2020, **10**, 4854–4862.
30 F. Li, Y. C. Li, Z. Wang, J. Li, D.-H. Nam, Y. Lum, M. Luo, X. Wang, A. Ozden and S.-F. Hung, *Nat. Catal.*, 2020, **3**, 75–82.
31 Y. C. Li, Z. Wang, T. Yuan, D.-H. Nam, M. Luo, J. Wicks, B. Chen, J. Li, F. Li and F. P. G. De Arquer, *J. Am. Chem. Soc.*, 2019, **141**, 8584–8591.
32 Z. Wang, Y. Li, X. Zhao, S. Chen, Q. Nian, X. Luo, J. Fan, D. Ruan, B.-Q. Xiong and X. Ren, *J. Am. Chem. Soc.*, 2023, **145**, 6339–6348.
33 M. Luo, Z. Wang, Y. C. Li, J. Li, F. Li, Y. Lum, D.-H. Nam, B. Chen, J. Wicks and A. Xu, *Nat. Commun.*, 2019, **10**, 5814.
34 C. Deacon-Price, N. Chen, A. Lal, P. Broersen, E. J. Meijer and A. C. Garcia, *ChemCatChem*, 2025, e202401332.
35 X. Wang, A. Xu, F. Li, S.-F. Hung, D.-H. Nam, C. M. Gabardo, Z. Wang, Y. Xu, A. Ozden and A. S. Rasouli, *J. Am. Chem. Soc.*, 2020, **142**, 3525–3531.
36 W. Ma, X. He, W. Wang, S. Xie, Q. Zhang and Y. Wang, *Chem. Soc. Rev.*, 2021, **50**, 12897–12914.
37 C. Chen, Y. Li, S. Yu, S. Louisia, J. Jin, M. Li, M. B. Ross and P. Yang, *Joule*, 2020, **4**, 1688–1699.
38 F. A. Rollier, V. Muravev, N. Kosinov, T. Wissink, D. Anastasiadou, B. Ligt, L. Barthe, M. C. Figueiredo and E. J. Hensen, *J. Mater. Chem. A*, 2025, **13**, 2285–2300.
39 P. Guo, K. Liu, X. Liu, R. Liu and Z. Yin, *Energy Fuels*, 2024, **38**, 5659–5675.
40 A. Vasileff, C. Xu, Y. Jiao, Y. Zheng and S.-Z. Qiao, *Chem*, 2018, **4**, 1809–1831.
41 G. Lee, A. S. Rasouli, B.-H. Lee, J. Zhang, D. H. Won, Y. C. Xiao, J. P. Edwards, M. G. Lee, E. D. Jung and F. Arabyarmohammadi, *Joule*, 2023, **7**, 1277–1288.
42 S. Ma, Y. Kim, Z. Zhang, S. Ren, C. Donde, L. Melo, A. S. Williams, M. Stolar, E. R. Grant and C. P. Berlinguette, *ACS Energy Lett.*, 2024, **9**, 2326–2332.
43 Y. C. Li, G. Lee, T. Yuan, Y. Wang, D.-H. Nam, Z. Wang, F. P. García de Arquer, Y. Lum, C.-T. Dinh and O. Voznyy, *ACS Energy Lett.*, 2019, **4**, 1427–1431.
44 H. Song, C. A. Fernández, A. Venkataraman, V. D. Brandão, S. S. Dhingra, S. S. Arora, S. S. Bhargava, C. M. Villa, C. Sievers and S. Nair, *ACS Appl. Energy Mater.*, 2024, **7**, 1224–1233.
45 J. Lee, H. Liu and W. Li, *ChemSusChem*, 2022, **15**, e202201329.
46 B. N. Khiarak, G. T. da Silva, J. Crane, C. P. O'Brien, M. R. Pepe, C. M. Gabardo, V. Golovanova, F. P. García de Arquer and C. T. Dinh, *Angew. Chem.*, 2025, **137**, e202509975.
47 J. Wang, Z. Zhang, W. Wu, Y. Liu, B. Dong, Y. Wang and Y. Wang, *ACS Energy Lett.*, 2023, **9**, 110–117.
48 S. Ma, H. Hu, F. Shen, Z. Chen and J. Hu, *Small*, 2025, e11008.